


Article

Long-Range Correlations and Natural Time Series Analyses from Acoustic Emission Signals

Leandro Ferreira Friedrich ¹, Édiblu Silva Cezar ², Angélica Bordin Colpo ², Boris Nahuel Rojo Tanzi ²,
Mario Sobczyk ², Giuseppe Lacidogna ^{3,*}, Gianni Niccolini ³, Luis Eduardo Kostascki ⁴,
and Ignacio Iturrioz ²

¹ Department of Mechanical Engineering, Federal University of Pampa (UNIPAMPA),
Alegrete 97546-550, Brazil; leandrofriedrich@unipampa.edu.br

² Department of Mechanical Engineering, Federal University of Rio Grande do Sul (UFRGS),
Porto Alegre 90046-902, Brazil; ediblucezar@gmail.com (É.S.C.); angelica.colpo@ufrgs.br (A.B.C.);
boris.rojotanzi@ufrgs.br (B.N.R.T.); mario.sobczyk@ufrgs.br (M.S.); ignacio@mecanica.ufrgs.br (I.I.)

³ Department of Structural, Geotechnical and Building Engineering, Politecnico di Torino, 10129 Turin, Italy;
gianni.niccolini@polito.it

⁴ Engineering Post Graduation Program, Federal University of Pampa (UNIPAMPA),
Alegrete 97546-550, Brazil; luiskosteski@unipampa.edu.br

* Correspondence: giuseppe.lacidogna@polito.it

Abstract: This work focuses on analyzing acoustic emission (AE) signals as a means to predict failure in structures. There are two main approaches that are considered: (i) long-range correlation analysis using both the Hurst (H) and the detrended fluctuation analysis (DFA) exponents, and (ii) natural time domain (NT) analysis. These methodologies are applied to the data that were collected from two application examples: a glass fiber-reinforced polymeric plate and a spaghetti bridge model, where both structures were subjected to increasing loads until collapse. A traditional (AE) signal analysis was also performed to reference the study of the other methods. The results indicate that the proposed methods yield reliable indication of failure in the studied structures.

Keywords: acoustic emission; long-range correlations; natural time analysis; heterogeneous materials



Citation: Friedrich, L.F.; Cezar, É.S.; Colpo, A.B.; Tanzi, B.N.R.; Sobczyk, M.; Lacidogna, G.; Niccolini, G.; Kostascki, L.E.; Iturrioz, I. Long-Range Correlations and Natural Time Series Analyses from Acoustic Emission Signals. *Appl. Sci.* **2022**, *12*, 1980. <https://doi.org/10.3390/app12041980>

Academic Editor: Kanji Ono

Received: 27 November 2021

Accepted: 11 February 2022

Published: 14 February 2022

Publisher's Note: MDPI stays neutral with regard to jurisdictional claims in published maps and institutional affiliations.



Copyright: © 2022 by the authors. Licensee MDPI, Basel, Switzerland. This article is an open access article distributed under the terms and conditions of the Creative Commons Attribution (CC BY) license (<https://creativecommons.org/licenses/by/4.0/>).

1. Introduction

Damage processes in heterogeneous material remains an open research problem. Classical theoretical methods rely on treating the material as a continuum, where macro parameters are regularized to facilitate the application of differential analysis, such as using homogenization [1–3] or plasticity-inspired damage theories [4–6]. However, this approach contradicts experimental evidence, which shows that the process is spasmodic and has evident discontinuity patterns. Thus, even if these methods yield satisfactory results in some instances, much rich information is also missed regarding the inherent discontinuities that are involved in heterogeneous-material structures. In contrast, other strategies focus directly on the information contained in the spatial-temporal distribution of discontinuities. Probably, the first one is the inspiring Bundle Model that was proposed by Daniels, 1945 [7] and nowadays explored by Hansen & Prhadhan, 2015 [8]. This approach essentially consists of a set of thin rods (a “bundle”) with random resistance levels that are subject to crescent loads. The evolution of the damage within the set is represented by the number of rods breaking with time, indicating the system’s behavior as it approaches catastrophic failure. Other inherently discrete methods that include the possibility of failure include meshfree methods, peridynamics, and the discrete element method. For an excellent revision regarding these approaches, refer to Jenabidehkordi, 2019 [9].

Acoustic emission (AE) techniques have been developed since the 1940s to monitor damage processes in structures, especially those that are built from heterogeneous material [10]. It consists of detecting the elastic waves that are produced by abrupt changes

inside the material (rupture, dislocation, among other causes) using sensors on the surface's structure. Each "waves' source" is called an event. The register of an event in an AE sensor is a signal or hit. Notice that there is no guarantee that an isolated signal informs of only one event since the waves from different events can affect the sensor simultaneously. Damage evolution is represented by the spatial-temporal distribution of the events, identified by a series of global parameters that are calculated from these signals, the most popular one being called *b*-value. This parameter could be related to the fractal dimension where the damage develops [11], being regarded in several works as a reliable precursor for the collapse, such as in Carpinteri et al. [12–14]. Other parameters are also used with the same goal. See, for instance, Alava and Zapperi 2006 [15] and Xu et al., 2021 [16].

There is an identifiable pattern in complex systems in several science fields as they come close to instability, as illustrated by Wilson, 1979 [17] with the normalization group theory. This method's central idea is that when a system approaches its critical collapse, its associated process has characteristics that do not depend on its geometry and boundary conditions because all scales are activated. This fact is observed in economics [18,19], solid-state physics [20], and mechanical systems [21], among other fields.

Several AE parameters present typical behavior that indicates when a system is close to its critical state. In this work, we investigate the behavior of long-range correlations of the temporal series that are studied using rescaled range (R/S^*) analysis (or Hurst method-*H*) [22] and detrended fluctuation analysis (DFA) [23]. In addition, we analyze the temporal series using the natural time (NT) domain, a tool that was introduced by Varotsos et al., 2001 [24] and subsequently employed by Potirakis et al., 2013 [25].

These two approaches are used to analyze AE signals in two examples from previous works which employed classical AE techniques. First is a polymer plate that is reinforced by glass fibers that was studied by Friedrich et al., 2020 [26]. The second was previously analyzed by Tanzi et al., 2021 [27] and consisted of a spaghetti bridge structure that was built from spaghetti sticks and monitored while the structure was loaded up to reach the failure. The proposed parameters from the AE signals are of interest, not only because of their potential as precursors of failure in the studied systems but also because they illustrate their underlying principle: all systems present the same basic patterns when they approach criticality. As shown in this work, this feature is an effective alternative to identify damage in structures.

Notice that the purpose of the present work is to present the parameters that are related to DFA, R/S^* , and NT analyses, which could be used in a concomitant way with other strategies of analysis that are used nowadays. The focus here is different from applying the DFA, R/S^* , and NT analyses to practical engineering problems. Our goal is to explore the sensibility of the cited parameters as precursors of the critical regime.

2. Theoretical Background

This section presents a brief description of the global AE parameters that are discussed here. The first one is the *b*-value, a classic approach that serves as a reference for the analyses that are provided through the proposed methods. Of the latter, two are long-range correlation measures: the detrended fluctuation analysis (DFA) and the rescaled range (R/S^*) or Hurst Analysis. The third one is the natural time approach.

2.1. *b*-Value Analysis

AE data analysis can be based on several criteria: signal amplitude, duration, rise time, acoustic emission energy, and number of AE signals. One of the most used is the *b*-value, which is calculated from the AE amplitude distribution data by the power-law relationship between the number of events (N) that exceeds a given amplitude (A) and the amplitude of these events [28]. This relationship is commonly known as Gutenberg–Richter [29]:

$$N(\geq A) \propto A^{-b} \tag{1}$$

Figure 1 illustrates how the b -value varies during a typical damage process. According to Aki [11] and Carpinteri et al. [12,30], its physical meaning is related to the fractal dimension (D) of the domain from which the cracks emanate through the expression $D = 2b$.

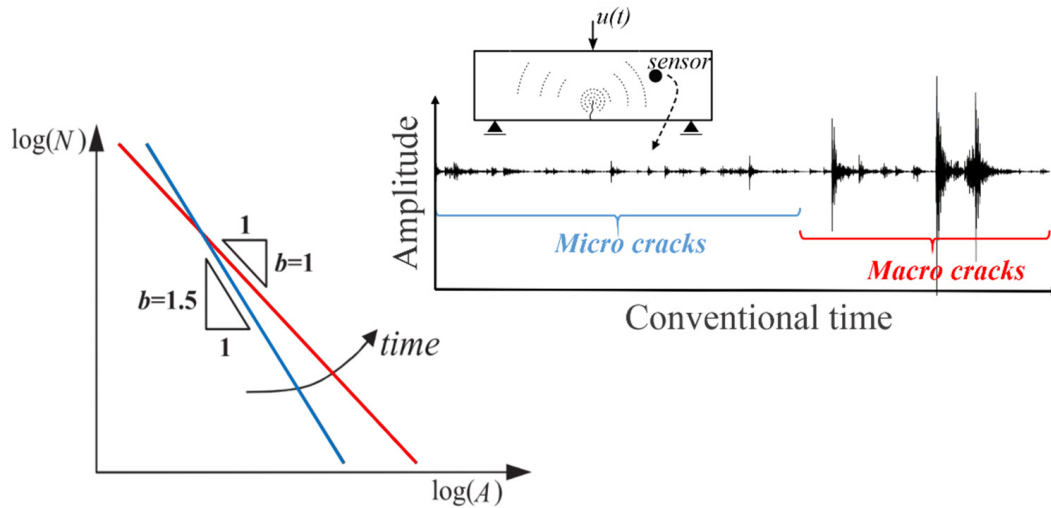


Figure 1. The b -value evolution and its physical meaning with respect to an acoustic emission signal.

At the beginning of the damage process, high b -values point out the occurrence of many small-amplitude AE events that are caused by micro-crack formation distributed throughout the whole structure’s volume, implying $D = 3$ and $D = 1.5$. As the damage process evolves to produce the localization effect, i.e., events tend to emanate from a preferential region and form a “cloud” of micro-fissures [26]. Thus, macro-crack nucleation occurs, and the acoustic events tend to originate from a definite surface, i.e., $D = 2$ and $D = 1$. In terms of Equation (1), this is interpreted as an increment of high-amplitude events. The b -value is a classic parameter in structural monitoring, and therefore, it is used here as a reference for evaluating the proposed indexes’ usefulness.

2.2. Long-Range Correlations Measures (DFA and Hurst)

Complex systems appear in many sciences, in topics as varied as heart rate dynamics, DNA, neuron spiking, meteorology, human motor activity, seismic signals, and economic time series [31,32]. These systems are characterized by distinct effects such as nonlinearity, spontaneous order, and adaptation, among others, and can be studied through fractal properties [33,34]. In AE signals such as those in Figure 2, interpreting events as irregularities in a time series, their occurrence can be identified through the series properties, such as self-similarity and scale-invariance. For instance, long-range power-law correlations are present if a time series exhibits scale-invariant features [35,36]. The strength or persistence of such long-range correlations helps to unravel or explain data behavior [35]. There are several methods to assess and quantify the strength of these correlations. This work uses two: detrended fluctuation analysis (DFA) and rescaled range analysis (R/S^*).

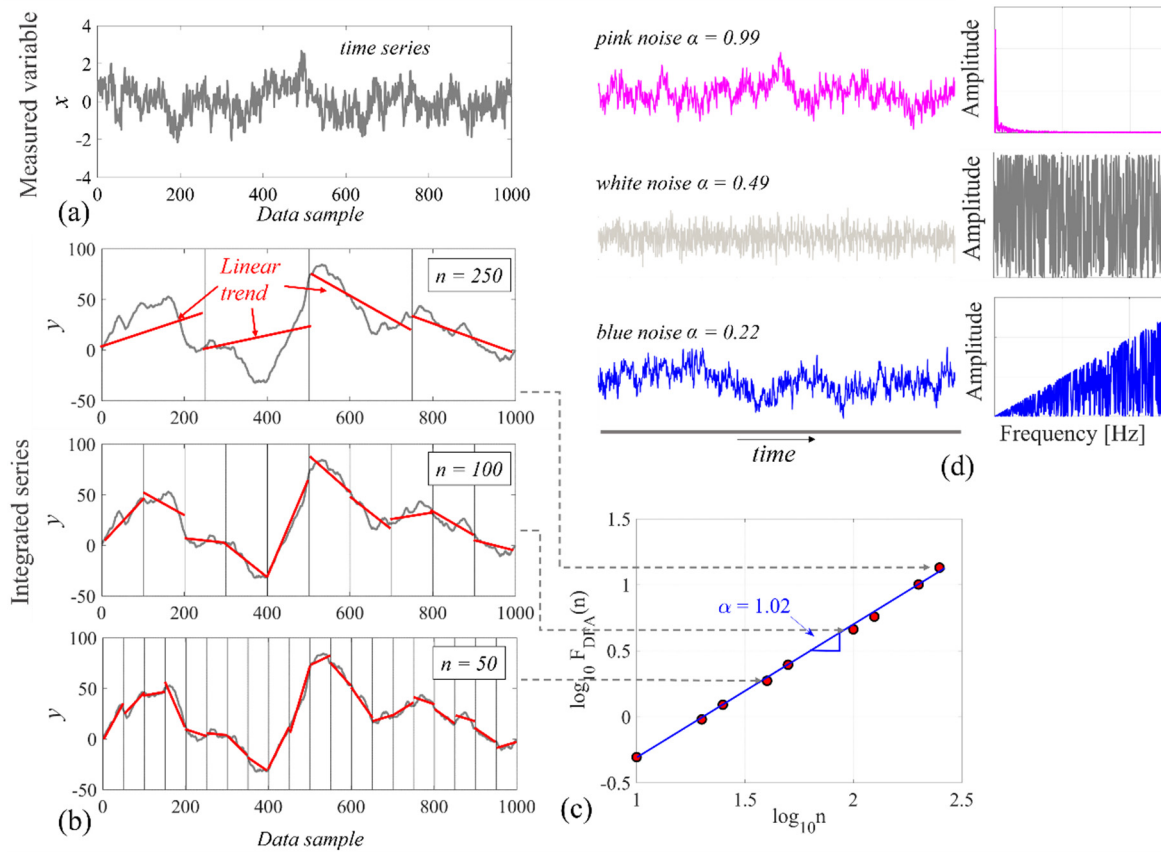


Figure 2. Graphical illustration of the DFA steps. (a) Example of time series; (b) integrated series divided into different size windows with their corresponding linear-fit trends; (c) log-log plot of average fluctuations $F_{DFA}(n)$ versus window sizes n . The estimated scaling exponent α is the slope of the least-squares fitted line; (d) representative examples of white (random), pink (fractal, long-range correlated, slightly persistent), and blue (anti-persistent) time and power-spectrum series. (Adapted from ref. [37]).

The DFA is a method that was initially proposed by Peng et al., 1994 [23] to detect long-range correlations in time series with non-stationaries [34,36,38–40]. Briefly, DFA fits a power law for estimating α , which is a measure of long-range correlations. It is calculated by plotting in log-log axes the average fluctuations in the series, named F_{DFA} , over different sampling scales (window sizes): α corresponds to the angular coefficient in the linear fit of F_{DFA} versus windows size. Figure 2 exemplifies the application of the DFA method for a time series in the form $\{x(i)\}_{i=1}^{N_{max}}$, where N_{max} is the total number of points in the series, in the case of a signal series $x(i)$ with $N_{max} = 1000$, Figure 2a. The general steps for applying the DFA are as follows [23,34,41]:

1. Integrate the series $x(i)$, obtaining $y(k) = \sum_{i=1}^k x(i) - \langle x \rangle$, where $k = 1, \dots, N_{max}$ and $\langle x \rangle$ stands for the average of x , see Figure 2b.
2. Divide $\{y(k)\}_{i=1}^{N_{max}}$ into non-overlapping windows of equal length n .
3. For each n -size window, fit a least-squares line to the integrated signal $y(k)$ (red line in Figure 2b). The sequence of fitted lines constitutes the trend series $y_n(k)$. Figure 2b shows the integrated series with three different window sizes, $n = 250$, $n = 100$, $n = 50$.
4. Calculate the average fluctuation F_{DFA} of the integrated series $y(k)$ around the trend series $y_n(k)$. Explicitly, $F_{DFA}(n) = \sqrt{(1/N_{max}) \sum_{k=1}^{N_{max}} [y(k) - y_n(k)]^2}$.
5. Repeat step 4 for a broad range of scales (sizes of n) to provide a relationship between F_{DFA} and n , i.e., $F_{DFA}(n)$.

- Plot $\log F_{\text{DFA}}(n)$ versus $\log(n)$ (see Figure 2c). If there is an obvious linear relationship between them, the slope of its least-squares fit estimates the scaling exponent α .

As explained in detail in [34,37], applying the DFA methodology yields both a measure of persistence and an index of self-similarity in the time series. In short, $\alpha \approx 0.5$ indicates that the signal is uncorrelated or non-similar in variability structure, as in the case of white noise (Figure 3d). If the signal's variability structures are long-range correlated, persistent, or self-similar, i.e., if a small-amplitude signal sample is very likely to be followed by an even smaller one (or similarly, if a large-amplitude sample tends to be followed by an even larger one), one finds $\alpha > 0.5$. That is the case with pink noise. Finally, if $\alpha < 0.5$, signal correlation is anti-persistent (the blue noise in Figure 3d): a small-amplitude sample is more likely followed by a large-amplitude one, and vice-versa.

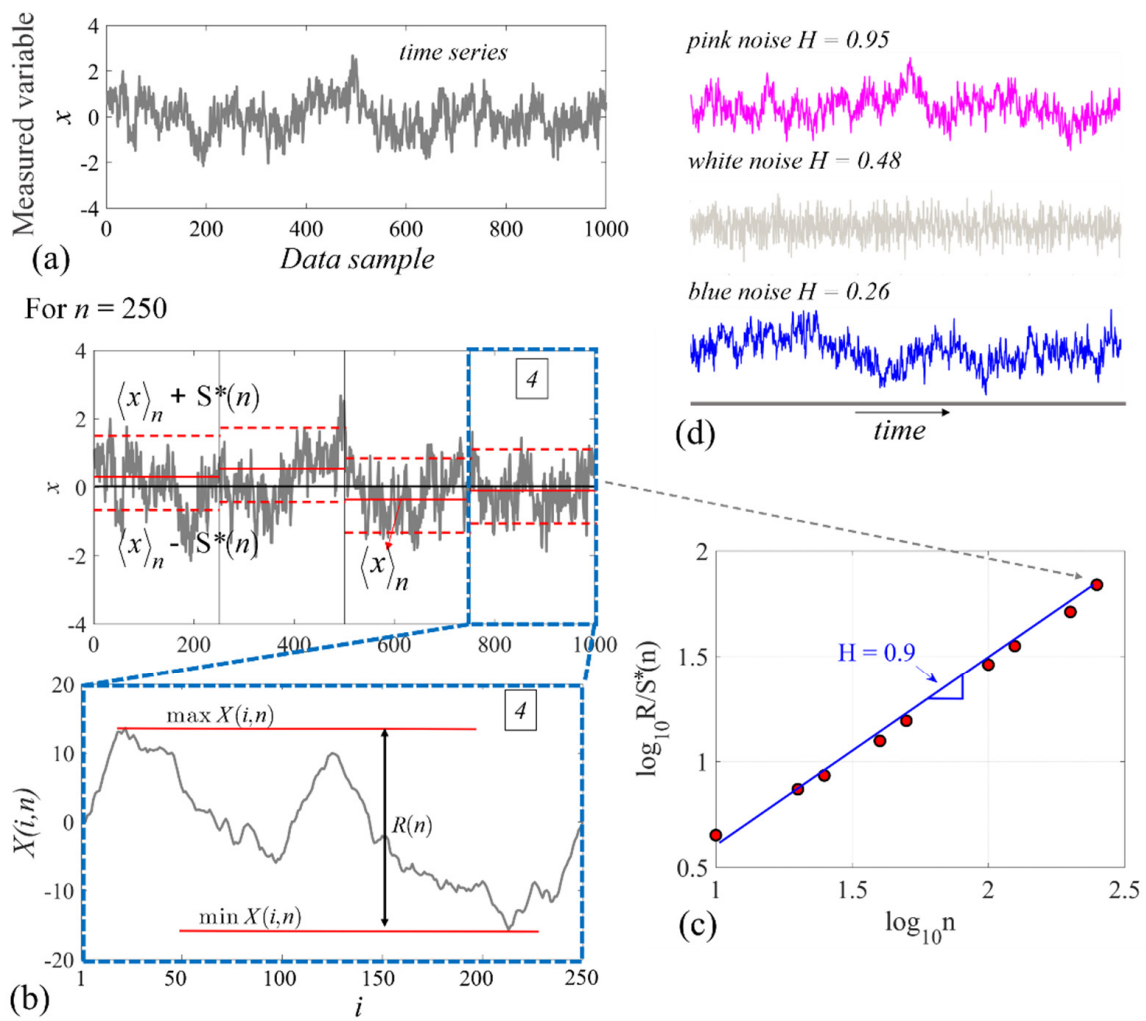


Figure 3. Basic parameters involved in standard R/S^* analysis: (a) a non-stationary time series $x(i)$; (b) Example of Hurst exponent considering $n = 250$, where $\langle x \rangle$ is the mean and $S(n)$ the standard deviation, $X(i, n)$ are the local differences accumulated from the mean, and $R(n)$ is the local range, that is, the difference between maximum and minimum $X(i, n)$ (adapted from [42]); (c) log-log plot of the rescaled range R/S^* versus window size n . The estimated scaling exponent H is the slope of the least-squares fitting line; (d) representative examples of H value for a white (random), pink (fractal, long-range correlated, slightly persistent), and blue (anti-persistent) time series.

The so-called R/S^* analysis is also a classic approach to evaluate the persistence or self-similarity of a signal. This methodology was introduced by Hurst [22], an English hydrologist, in an extensive series of empirical studies involving the flow of the Nile River. Its basic idea is to determine how the range of the cumulative fluctuations depend on the length of the data subset under analysis [42], being illustrated in Figure 3 for the same time series that was discussed in Figure 2a, considering windows with size $n = 250$ [43]. As in the DFA method, a time series of length N_{\max} is divided into equal-length windows with size n . Next, for each window:

1. Take the mean $\langle x \rangle_n = (1/n) \sum_{j=1}^n x(j)$ of the n -th window, marked as the solid red lines in Figure 3b.
2. Sum the differences from the mean to get the cumulative total $X(i, n)$ at each data point, from the beginning of the period to any desired point, i.e., $X(i, n) = \sum_{i=1}^n (x(i) - \langle x \rangle_n)$, Figure 3b.
3. Calculate the local range $R(n) = \max X(i, n) - \min X(i, n)$ as the maximum fluctuation of the sum of the deviation from the mean, where $\max X(i, n)$ and $\min X(i, n)$ are the maximum and minimum values of $X(i, n)$, respectively, and $1 \leq i \leq n$ (Figure 3b).
4. Take the standard deviation $S^*(n) = \sqrt{(1/n) \sum_{i=1}^n [x(i) - \langle x \rangle_n]^2}$ over the window to normalize the range relative to the input fluctuations in the series (dashed red lines in Figure 3b).
5. Rescale the range, that is, calculate $R(n)/S^*(n)$.
6. Finally, calculate the mean value of the rescaled range for all windows, n_w (four in the case of Figure 3b):

$$(R/S^*)_n = \frac{1}{n_w} \sum_{m=1}^{n_w} R_m/S^*_m \tag{2}$$

For windows with different lengths, the new dimensionless value R/S^* is well described by the following empirical relation, as illustrated in Figure 3c:

$$(R/S^*)_n \sim n^H \tag{3}$$

In log-log axes, the slope of a least-squares regression is the estimate of the Hurst exponent H .

The parameter H varies from 0 to 1 and has the same meaning as the α parameter (Figure 3d): $H \approx 0.5$ for the case of white noise, i.e., uncorrelated; $H > 0.5$ if the process is persistent; and for an anti-persistent case, $H < 0.5$. Moreover, it also expresses the time series' fractal dimension (d) from the relation $d = 2 - H$, where $1 < d < 2$ [44]. Thus, $d \rightarrow 1$ for persistent correlations, i.e., the series tends to a line, whereas it tends to a plane for anti-persistent correlations ($d \rightarrow 2$).

About the two methodologies described above, α and H , some considerations are in order:

- Although this work is focused only on first-order fitting functions, as suggested in [43], higher-order fitting curves can also be used.
- Window sizes must be limited to avoid significant linearity variations in $(F_{\text{DFA}}(n) - n)$ and $(R/S^* - n)$. According to [45] and [46], the windows used here vary from $n_{\min} = 10$ for the smallest to $n_{\max} = N_{\max}/4$ for the largest.

2.3. Natural-Time Analysis

The analysis in the natural time domain allows identifying when a complex system enters a critical state [47]. For a time series comprising N events, the natural time χ_k of the k -th event is defined as this event normalized, divided by the total number of the considered events, $\chi_k = k/N$ [2], see Figure 4. On the other hand, natural time χ_k serves as an index for the occurrence of the k -th event, Figure 4. It is, therefore, smaller than, or equal to, unity (0,1) [44,48]. We denote by Q_k a quantity proportional to the energy of the individual k -th event, so its normalized energy is given by $p_k = Q_k/\sum_{n=1}^N Q_n$. In

the specific case of AE, Q_k could be the signal energy measured in defined form or also the signal magnitude that will relate with the signal energy. In natural time analysis, the evolution of the pair (χ_k, p_k) is considered [44], see Figure 4.

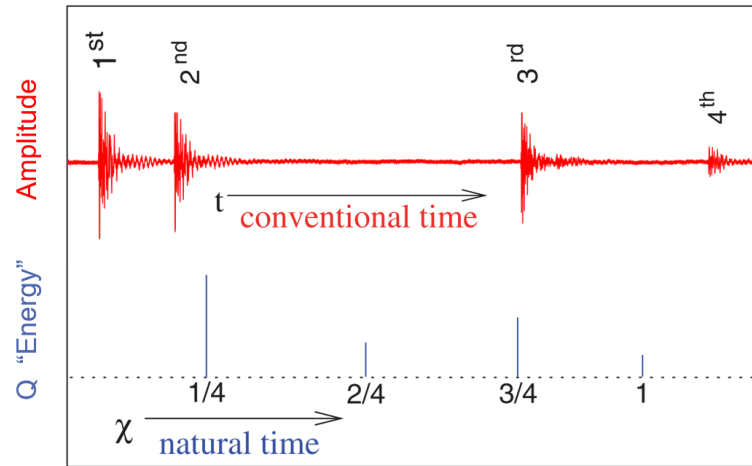


Figure 4. Natural time in the context of acoustic emission time series (adapted from ref. [48]).

The natural time χ_k 's variance κ_1 is given by:

$$\kappa_1 = \langle \chi^2 \rangle - \langle \chi \rangle^2 \equiv \sum_{k=1}^N p_k \left(\frac{k}{N} \right)^2 - \left(\sum_{k=1}^N \frac{k}{N} p_k \right)^2 \tag{4}$$

κ_1 varies when a new k -th event occurs, once natural time χ_k changes from k/N to $k/(N + 1)$ and p_k changes to $Q_k / \sum_{i=1}^N Q_i$. The called order parameter κ_1 may identify the approach of the dynamical system to a critical point [48,49].

Moreover, the entropy (S) in natural-time domain is defined as,

$$S = \langle \chi \ln \chi \rangle - \langle \chi \rangle \ln \langle \chi \rangle \equiv \sum_{k=1}^N p_k \chi_k \ln \chi_k - \left(\sum_{k=1}^N p_k \chi_k \right) \ln \left(\sum_{k=1}^N p_k \chi_k \right) \tag{5}$$

Notice that the entropy in natural time refers to numerical signal data and does not directly relate to the property from traditional thermodynamics [50], being related to the information theory instead [51]. Similar to the variance κ_1 , the entropy S is also a dynamic parameter depending on the sequential order of events [52].

The third variance term that is considered in this method is the time-reversal entropy S_{rev} . It is obtained by reversing the order of the energy data (Q_k), calculating S with this new series, and then subtracting the entropy from the original series from the result. According to Daniel et al., 2020 [53], this entropy parameter is the most sensitive one to the ordering of the signal data.

It is possible to evaluate another order parameter, which describes the “average” distance $\langle D \rangle$ between the curves of the normalized power spectrum of the events [48],

$$\Pi(\omega) = \left| \sum_{k=1}^N p_k e^{i\omega \frac{k}{N}} \right|^2 \tag{6}$$

where $\omega = 2\pi\phi$ ($\phi \in (0, 0.5)$ standing for the frequency in natural time) and the ideal normalized power spectrum, that is the normalized power spectrum when the sequence is in critical regime,

$$\Pi(\omega)_{ideal} = \frac{18}{5\omega^2} - \frac{6 \cos \omega}{5\omega^2} - \frac{12 \sin \omega}{5\omega^3} \tag{7}$$

if $\omega \rightarrow 0$, Equation (7) simplifies to $\Pi(\omega)_{ideal} \approx 1 - 0.07\omega^2$. When $\Pi(\omega)$ approaches $\Pi(\omega)_{ideal}$ from below, the critical state is indicated.

The application of the natural time method to analyze AE signals can be described with aid from Figure 5. First, the events/hits are separated from the overall signal, Figure 5a. Then, they are ordered in the natural time domain, that is, in terms of χ_k and Q_k (Figure 5b). Next, of the order parameters, κ_1 and $\langle D \rangle$, and the entropy measurements S and S_{rev} are calculated with Equations (4)–(7). Finally, according to Varotsos [54–56], the dynamic system is defined as in a true critical state (“ t_{crit} ” is achieved, see Figure 5c) if:

1. The “average” distance $\langle D \rangle$ becomes smaller than 10^{-2} .
2. The variance κ_1 , when descending from above, approaches 0.070;

The entropies S and S_{rev} are both smaller than the entropy of uniform noise $S_u = (\ln 2/2) - 1/4 \approx 0.0966$.

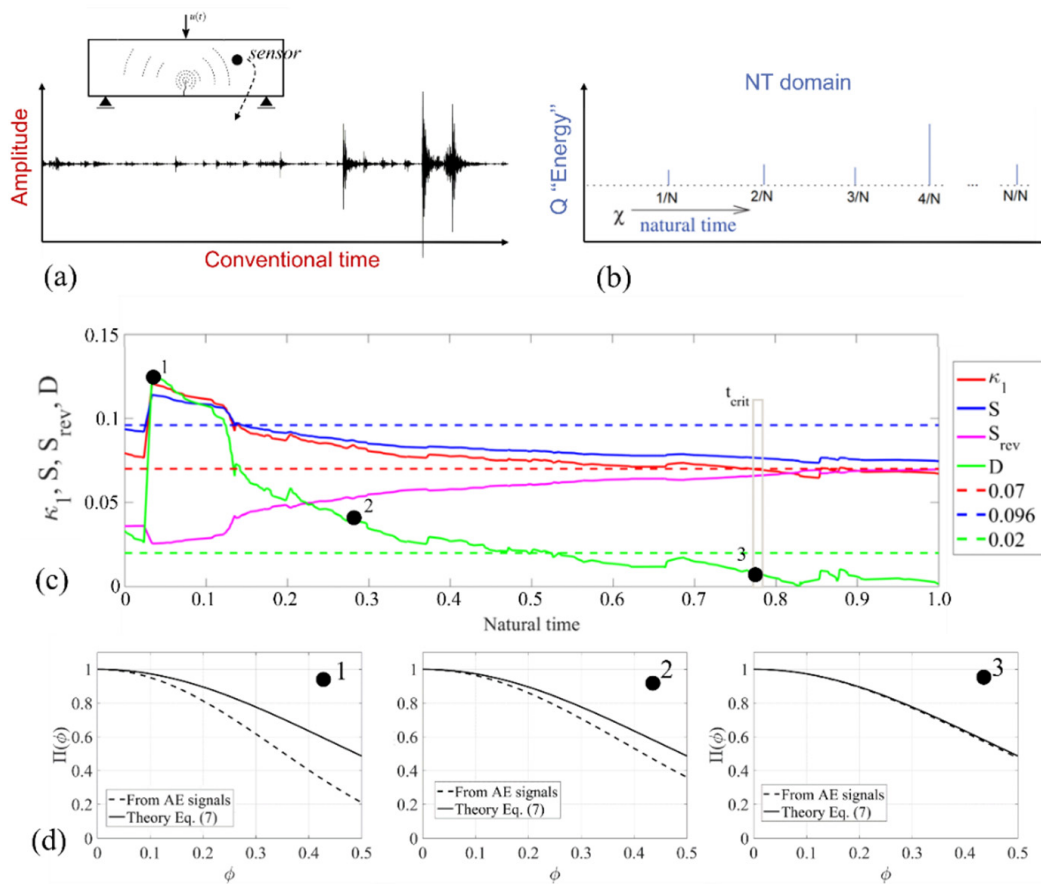


Figure 5. Applying the natural-time method: (a) a typical time series from AE signals; (b) series description in the natural time domain; (c) evolution of the order parameters and entropies in natural time. t_{crit} indicates the point of convergence of the criteria, where the structure enters a critical stage; (d) evolution of the normalized power spectrum until reaching t_{crit} .

Figure 5c shows an example of true coincidence, indicated as t_{crit} , where all the criteria that are listed above are met. Furthermore, in Figure 5d, a typical sequence of the normalized power spectrum is presented, where it is expected that as it approaches the critical stage, the obtained data (dashed lines) reach the analytical solution (solid lines). It has been observed that the instant of (true) coincidence may also be invariant with the chosen threshold value [57]. This possibility will also be explored in the applications that are described in Section 3.

3. Applications

3.1. Three-Point Bending Test of a Glass Fiber-Reinforced Polymeric Plate

3.1.1. Test Description

The first AE test was performed with a glass fiber-reinforced polymer (GFRP) specimen. GFRP is a resin compound with a glass fiber second layer, which provides high resistance to traction, flexion, and impact. There are several ways to manufacture GFRP specimens, see Ref. [58]. The one that was used here was laminated manually with fibers that were randomly arranged within its matrix, Figure 6a, but some of its parts have their fibers distributed along a preferential direction. This arrangement is similar to the one that was used by the company “IMAP Indústria e Comércio” [59] in the making of suspended-work baskets (Figure 6b). The material’s relevant properties are: modulus of elasticity $E = 74.5$ GPa and mass density $\rho = 1450.3$ kg/m³.

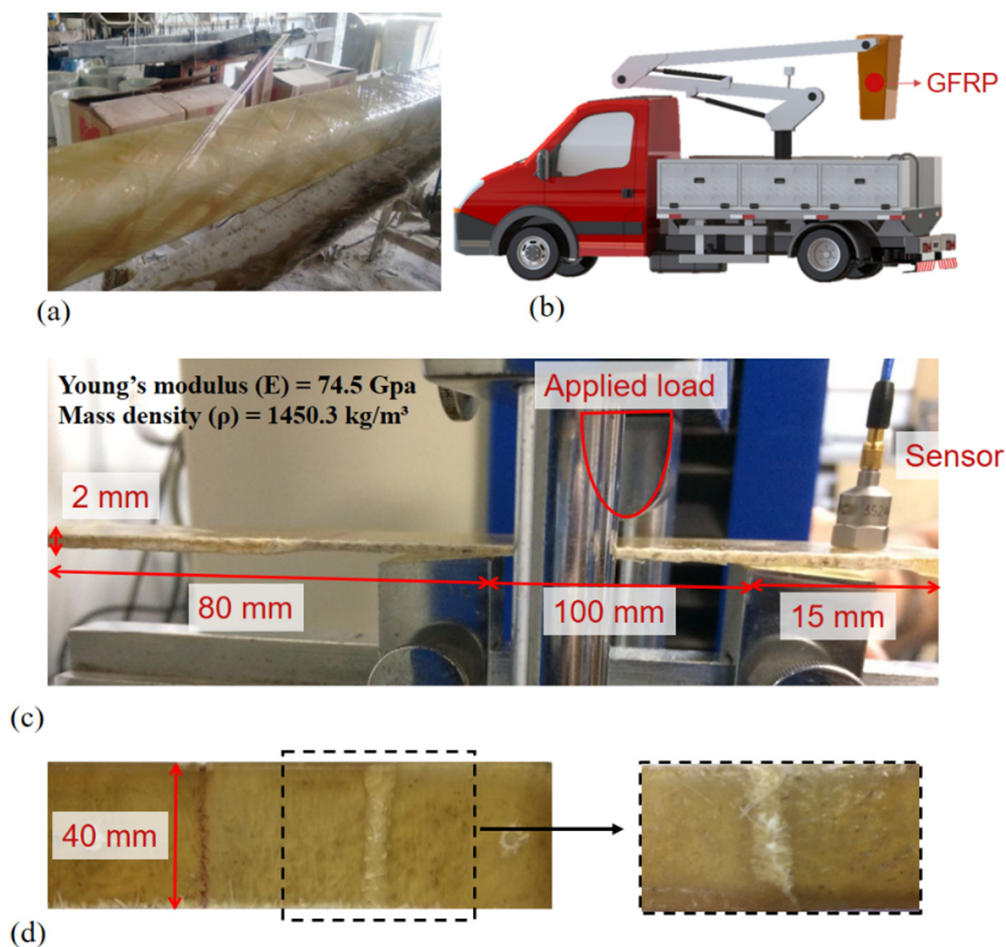


Figure 6. (a) Specimen manufacturing; (b) GFRP application example; (c) The sample dimensions and test conditions; (d) The ruptured specimen final configuration with a detailed view of the fracture.

The specimen was subjected to a three-point bending test (TPB). Figure 6c shows the test configuration, including the position of the piezoelectric sensor for acquiring the AE signals. For detailed information regarding the data acquisition for this application, refer to Friedrich et al., 2020 [26]. Figure 6d shows the rupture configuration of the tested specimen, with a detailed view of the fractured region.

3.1.2. Results

Figure 7a depicts the AE activity during the TPB test in normalized time (time/time_{peak}, where time_{peak} = 72 s is the peak loading time). Approximately 5050 signals above a 0.25 mV threshold level were separated throughout the TPB test according to the methodology that was described in [26]. The number of instantaneous and accumulated signals are presented in Figure 7b, accompanied by the evolution of the load (F/F_{max}) and the AE energy (E_{AE}/E_{AEmax}), which was computed as recommended in RILEM [60]. The results in the same figure indicate a considerable correlation between the AE energy and the number of accumulated signals. In addition, one identifies three distinct patterns throughout the test. The first occurred in the region 0–0.26, where a few sparse avalanches were identified. Their isolated nature suggests that they were probably caused by local effects, such as the specimen accommodation on its supports, without a significant change in the specimen stiffness. Within the 0.26–0.78 range, damage grew indistinctly throughout the structure, with low-amplitude AE signals from no particularly discernible source. Finally, cracking coalescence took place in the region 0.78–1.0. This was indicated by the increment in the signal avalanches, which can be considered a precursor to the imminent collapse in the structure.

The *b*-value was the reference parameter to the analyses that was performed through all methods that were considered in this work, and its calculation is described in Figure 7a. The test period was divided into 14 intervals, and the *b*-value was calculated for each of them [26]. Instead of repeating the expected pattern that is shown in Figure 1, it decreased locally in several opportunities as large-amplitude AE signals occurred throughout the process. That suggests that the rupture happened in spasms that were uniformly distributed along the whole process instead of abruptly, i.e., the energy dissipates in several small events instead of being stored to a large amount and released at once in an explosive collapse.

Figure 7c summarizes the corresponding AE signal long-range analysis according to the DFA and *R/S** methods. The DFA (blue points) and Hurst (pink points) exponents were evaluated for each event throughout the normalized test period, considering a 25-hit moving window, i.e., parameters were calculated at hit #25, based on a temporal series starting at hit #1, then from #2 to #26, #3 to #27 and so on. The dotted black transversal line separates the values of α and *H* indicating correlated/persistent signals (>0.5) from noncorrelated/anti-persistent ones (<0.5). The responses from both methods were similar. The persistence they indicated at the beginning of the test is probably related to the specimen accommodation on its supports, as already pointed out in Figure 7a. Then, both exponents tended about 0.5 until the normalized time 0.75 was reached. At this instant, both exponents presented significant fluctuations, which indicates the spasmodic behavior of the structure. That agrees with the findings in Skordas et al., 2020 [61], where the DFA method yielded exponents of about 0.6 (persistent behavior) for seismic signals that were acquired when large earthquakes were about to occur, then tending to 0.5 (random) after they occurred.

The evolution of natural-time parameters versus normalized time is plotted in Figure 7d. For this analysis, we follow the same reasoning as [47] and [62], taking the energy component (Q_k) as equal to $A_{\max,k}^{1.5}$, where $A_{\max,k}$ is the maximum amplitude of the signal, an approach commonly found also in seismology studies [63]. Calculation of $A_{\max}^{1.5}(t)$ (with *t* denoting the conventional time) was performed hit by hit, i.e., every time a new signal comes up, a new signal is included in the NT analysis, leading to the rescaling of the (χ_k , Q_k) time series and the recalculation of κ_1 , *S*, *S_{rev}* and $\langle D \rangle$. The results are shown in normalized time for easier identification of the possible entry point to a critical state, that is, the instant when criticality conditions, as described in Section 2.2 [64,65], are fulfilled. There are three such points that are indicated in Figure 7d. The first one occurred right before a dense region of AE events, at normalized time 0.24, with an abrupt change in the AE energy rate (see Figure 7b). The second was probably related to the consecutive avalanches that were observed between normalized instants 0.42 and 0.52 (notice the in-

crease of instantaneous hits in Figure 7b). Finally, there was a third and more extensive period (0.5288–0.5939) where parameters converge, which indicates the imminent structure collapse.

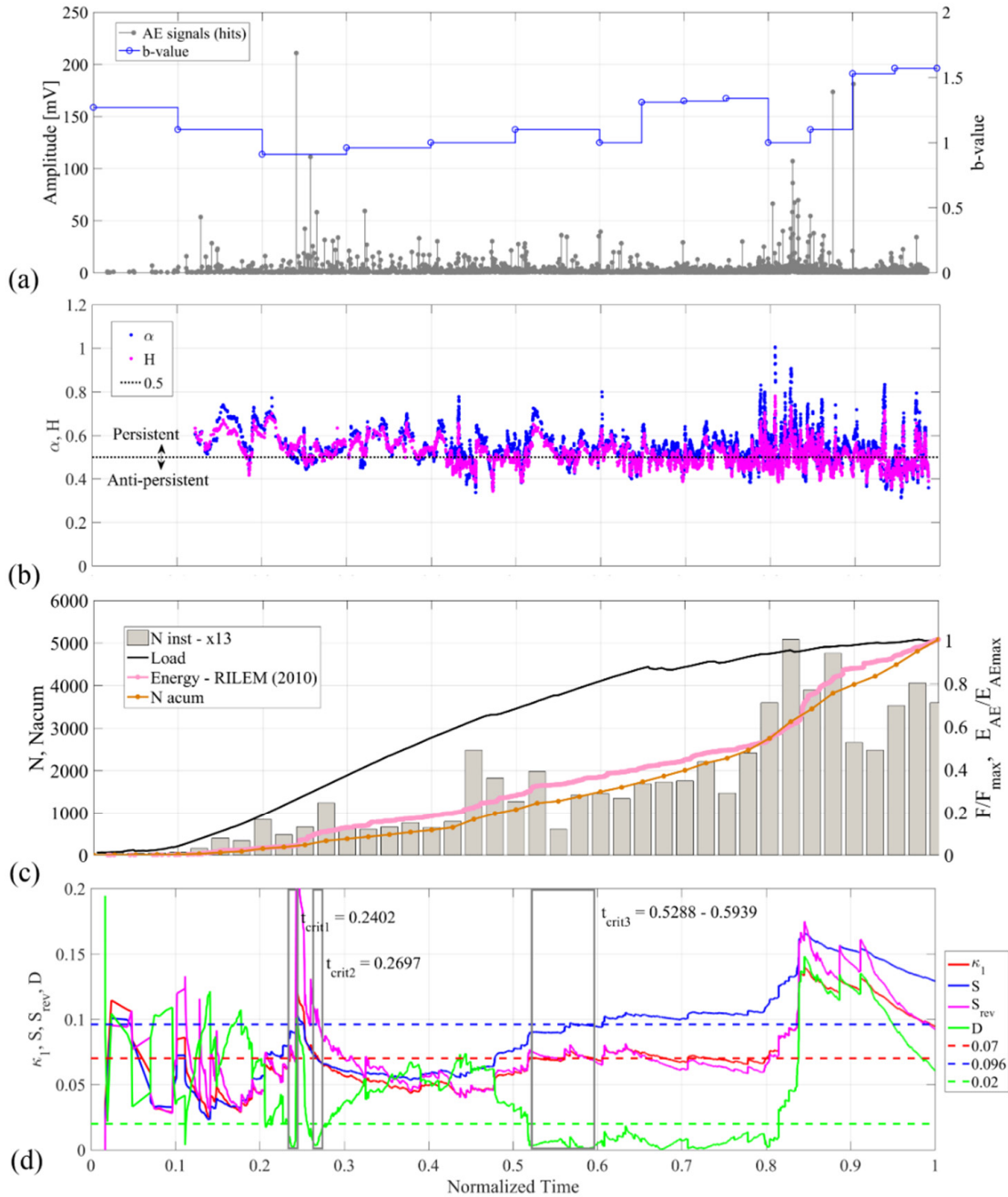


Figure 7. (a) AE signals with b -value analysis; (b) Number of instantaneous signals, number of accumulated signals, applied load, and accumulated energy versus normalized time. The first was multiplied by 13 to maintain the same vertical scale for instantaneous and accumulated signals; (c) Application of Hurst and DFA methods to the AE data; (d) NT analysis of the AE time series with threshold values $(A_{max}^{1.5})_{Th} = 0.25$ mV. The following auxiliary horizontal lines were added: $\kappa_1 = 0.070$ (dashed red), $\langle D \rangle$ limit = 10^{-2} (dashed green), entropy limit $Su \approx 0.0966$ (dashed blue).

3.1.3. Discussion

(i) Considering the DFA and Hurst parameters, there is no discernible parameter trend in Figure 7c to indicate criticality. These parameters' behavior can be clarified with the aid of Figure 8, illustrating the analysis of the exponents α and H for two signal samples, for instants 0.24 and 0.82. There are two discernible regions for each dataset, and the blue lines show their corresponding linear fits. However, this effect is masked if a single fit is calculated for the whole dataset (red line). This is a crucial difference because the two regions indicate different behaviors concerning time correlation: short-term correlations are persistent, whereas long-term ones are anti-persistent. Similar effects can be found in other works, such as Varotsos et al., 2003 [54], Lin et al., 2014 [66], and Silva et al., 2004 [67].

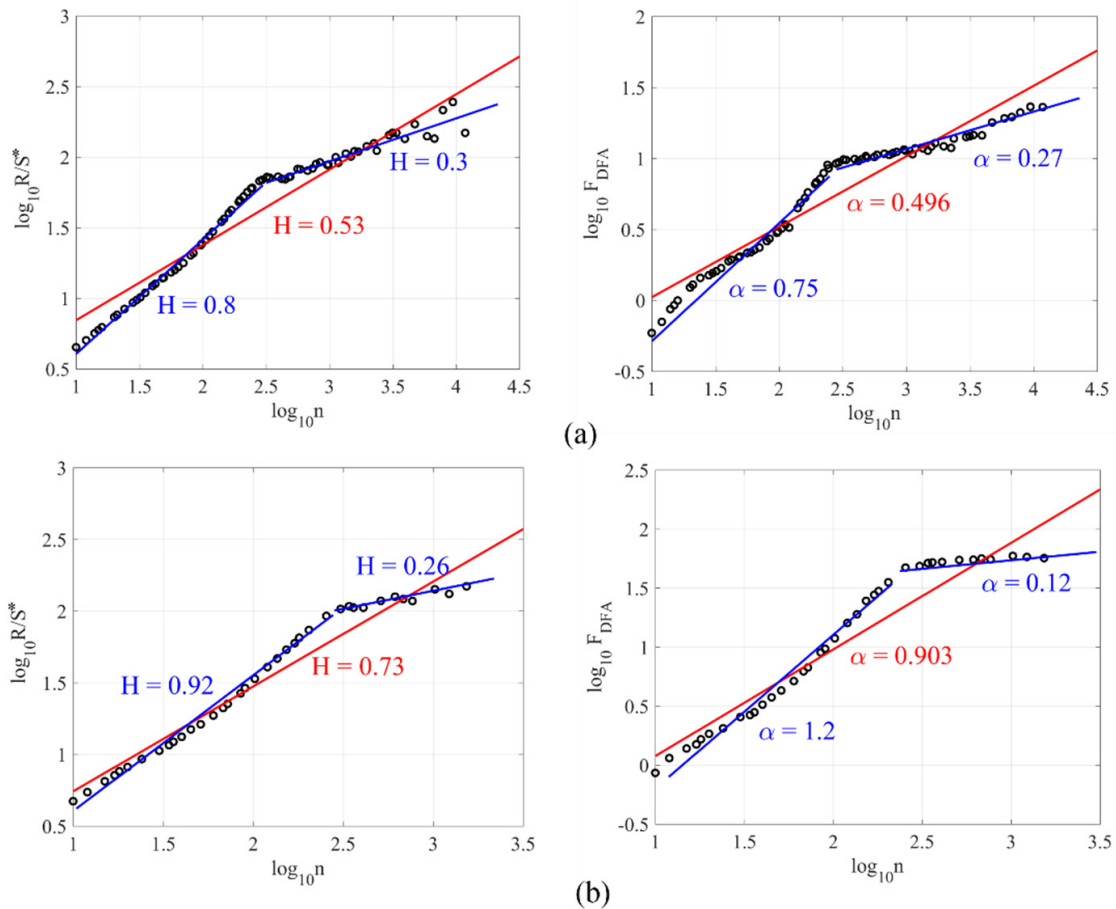


Figure 8. Details of the Hurst and DFA exponents for (a) signal at normalized time 0.24; (b) signal at normalized time 0.82.

To further explore this behavior, α was re-evaluated for short-term windows ($n < 300$) and long-term ones ($n \geq 300$), respectively designated α_{short} and α_{high} . The corresponding results are depicted in Figure 9, where a 100-point moving mean was added to (dotted line) improve tendency visualization in each region, in the same figure the load evolution (F/F_{max}) during the simulation in black line is presented.

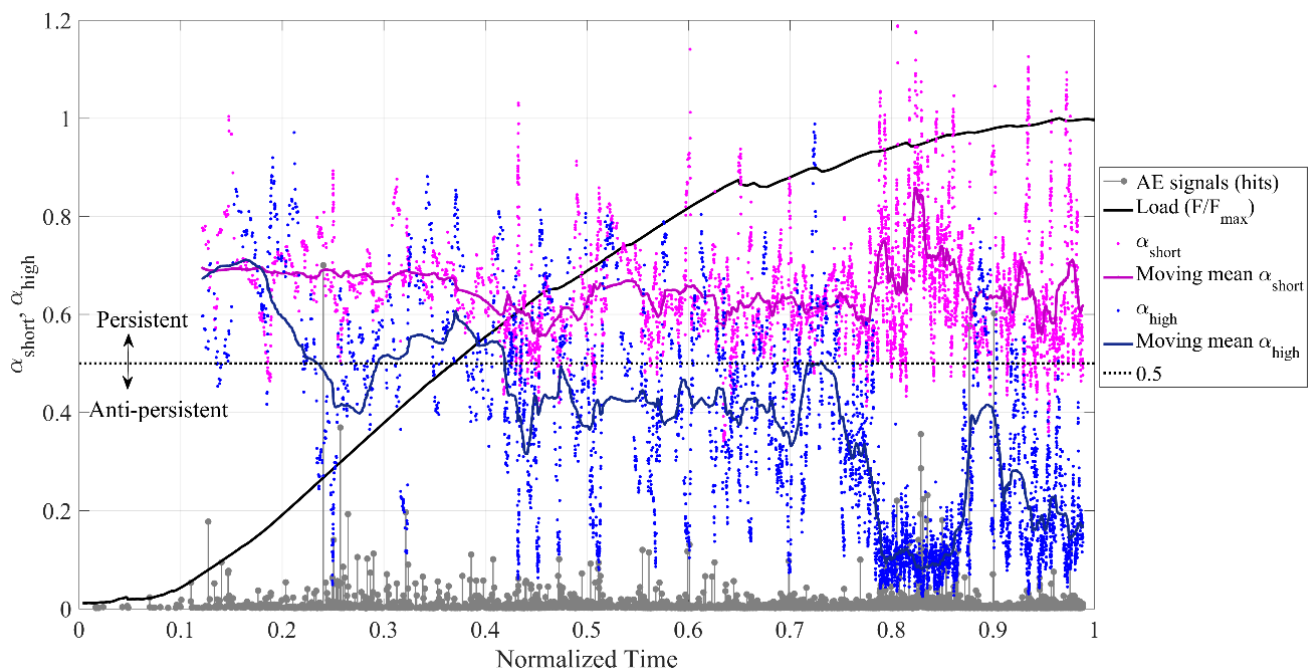


Figure 9. DFA considering short-term (α_{short}) and long-term (α_{high}) windows for the GFRP plate. The load and AE signals out of scale.

The correlation force for the short-term windows tends to be persistent throughout the entire test, increasing significantly between the normalized instants 0.78 and 0.88, which correspond to intense AE activity as the structure approaches collapse. During the same period, long-term correlation forces are nearly nil. This opposite convergence of α_{short} and α_{high} may indicate spasmodic behavior. A similar effect is also observed between instants 0 and 0.24: initially, both α_{short} and α_{high} have an approximated average of 0.7 until normalized instant 0.18. Then, α_{high} falls within the noncorrelated range (<0.5) that precedes an avalanche (see Figure 7a) with large-amplitude signals.

(ii) Regarding the natural time parameters that are presented in Figure 7d, it is necessary to check whether the identified critical points represent “true coincidence”, i.e., not only are all the criteria satisfied, but they are also invariant to the selected threshold. Applying the same methodology that is described in the previous section, two new threshold values are applied to separate hits from the overall AE signals: those with amplitudes that are higher than (a) 1 mV and (b) 2 mV. In the first case, the reconstructed time series comprises of 2832 events, whereas the second one has 1164. The corresponding results in natural time are given in Figure 10. Compared with Figure 7d, two critical points are confirmed for all the thresholds: the ones approximately at normalized times 0.27 and 0.59. As for the third possibly critical point that is identified in Figure 7c, it is not an actual critical point since it does not appear for the other two thresholds.

As mentioned earlier, the first critical state (0.27) is related to a dense region of AE signals between 0.42 to 0.52 of the normalized time, see Figure 7a,b, where the stiffness of the structure is affected as shown by the instability that is present in the load curve (see Figure 7a). The second point (0.59) indicates the critical stage preceding structure failure, which occurs about 30 s later. Additionally, κ_1 tends to stabilize at nearly 0.07 for normalized time 0.6, regardless of the selected three thresholds value for hit identification. That means that the system has started to self-organize, an obvious prerequisite for failure [68].

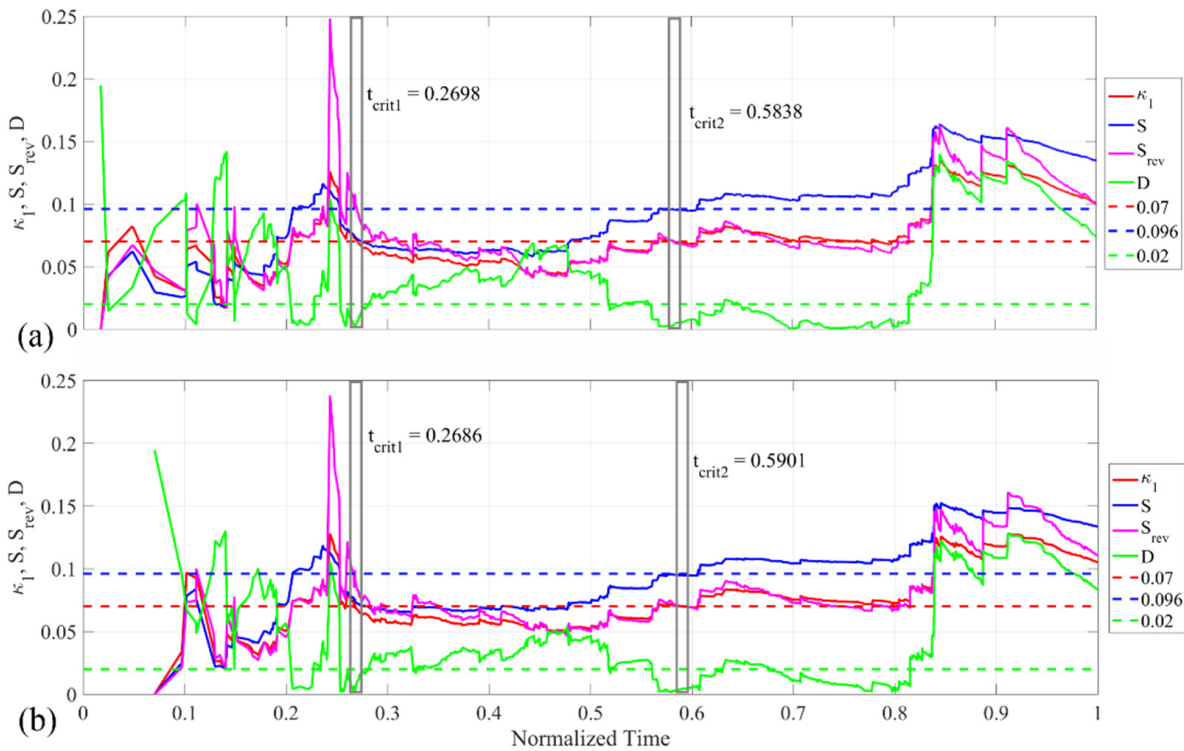


Figure 10. NT analysis of the AE time series for two threshold values $(A_{max}^{1.5})_{Th}$: (a) 1.0 mV and (b) 2.0 mV. For ease of interpreting the results, the values for $\langle S \rangle = 0.070$ (dashed red), $\langle D \rangle$ limit = 10^{-2} (dashed green), entropy limit $Su \approx 0.0966$ (dashed blue) are also depicted as horizontal lines.

A second approach to performing the NT analysis is to consider Q_k that equals the acoustic emission energy $E_{AE,k}$, as suggested in RILEM [60] and shown in Figure 11 for the original dataset (5050 signals, 0.25 mV threshold). Since the methodology for calculating the NT parameters is the same as in the case of Figure 10, these new data are presented according to the same standards.

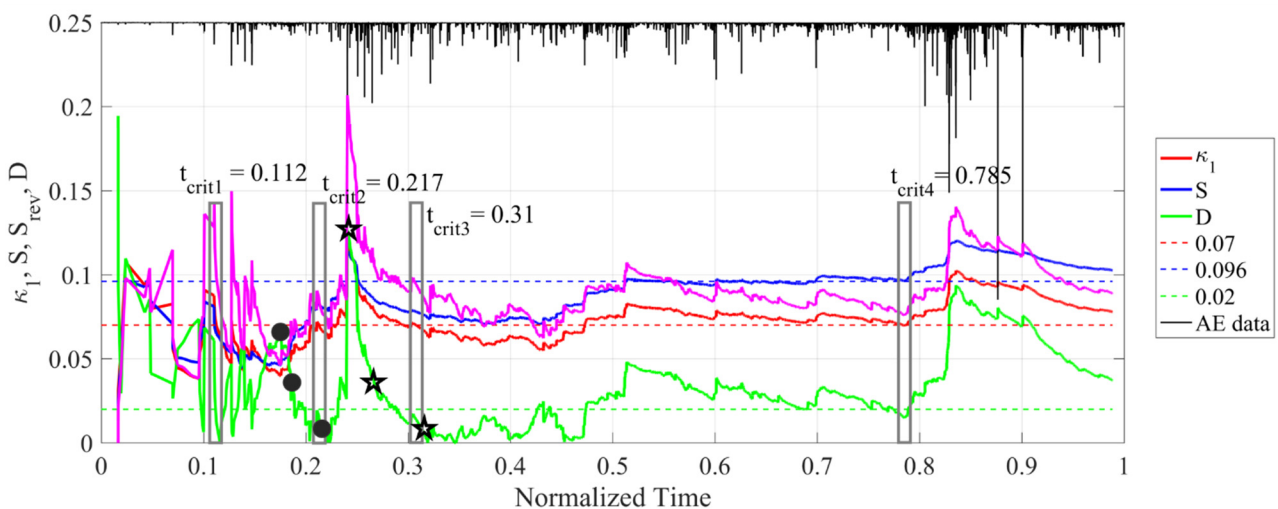


Figure 11. Natural time analysis of the AE events during the three-point bending test on the GFRP plate considering $Q_k = E_{AE,k}$.

In this case, we have four points of true coincidence. The first and second critical points precede the occurrence of large avalanches, that is, regions of considerable AE activity. The third point at 0.31 again indicates the approximation of a critical region (0.42, 0.52) of the normalized time, as already mentioned in the previous approach. Finally, the last point at 0.785 clearly represents the structure’s entry into a critical pre-failure stage. Thus, the analysis of the natural time using the AE signal energy also presents as a valid amount of energy (Q) to find the critical stages of the structure that are monitored by AE in the NT domain.

In Figure 11, the true coincidence points 2 and 3 were monitored to evaluate the behavior of the normalized power spectra $\Pi(\phi)$ versus the natural frequency (ϕ) relationship that was obtained by analyzing the series of signals, in comparison with the ideal estimate by Equation (7). For each point, we analyzed three normalized time instants prior to the critical time being reached, black circles and black stars, respectively. It can be seen in the results that are presented in Figure 12, that when approaching the point of true coincidence, the curves that are obtained from the series of AE signals, and those that were theoretically determined, approach from the bottom to the top. At the same time if we look at Figure 11, we notice that the value of κ_1 also approaches to 0.07, so both order parameters for criticality converge.

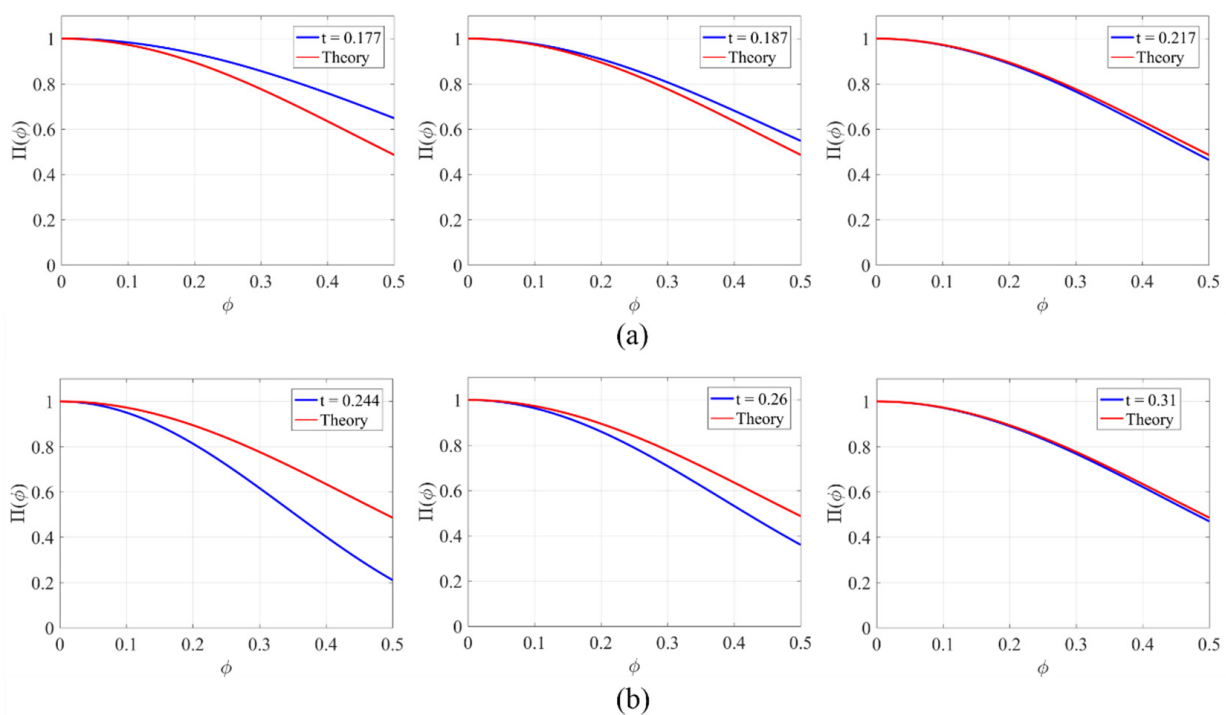


Figure 12. Evolution of $\Pi(\phi)$ of the AE activity, (a) critical time 2 (black circles— $t_{crit2} = 0.217$) and (b) critical time 3 (black stars— $t_{crit3} = 0.31$).

3.2. “Spaghetti” Bridge Model

3.2.1. Test Description

The same analysis methods that were proposed here were applied to another AE dataset that was obtained from the spaghetti bridge that is depicted in Figure 13a. This bridge was built in 2018 by undergraduate engineering students to take part in the contest at the Engineering School of Federal University of Rio Grande do Sul (UFRGS), which has occurred twice a year since 2004. Detailed information regarding the contest is given in [69], and all the appropriate steps for acquiring the corresponding AE data are described in Tanzi et al., 2021 [27].

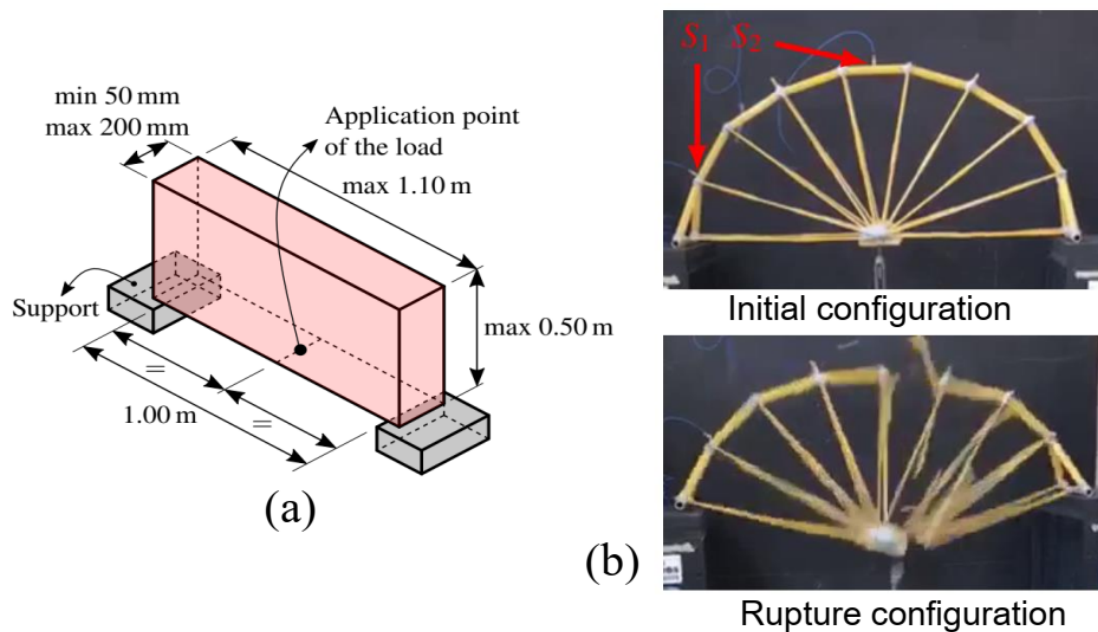


Figure 13. “Spaghetti” Bridge Model: (a) Geometric restrictions for the contest, (b) The initial and final configurations of the bridge during the test (Adapted from ref. [27]).

3.2.2. Results

The “Spaghetti” bridge model results throughout the loading test are shown in Figure 14. For a threshold level of 0.7 mV, the AE sensors detected 230 signals, Figure 14a. These results appear in Figure 14b as the numbers of instantaneous and accumulated signals, the loading evolution (F/F_{\max}), and the acoustic emission energy ($E_{\text{AE}}/E_{\text{AEmax}}$) against the normalized time. For this test, signals occur nearly when the load increases, indicating that their distribution depends explicitly on the loading pattern. Additionally, up to $t \approx 0.6$, signal counts grow at an approximately constant rate. Then, there is a sharp increase in the number of signals for a brief period. After that, the signal counts grow once again at a nearly constant rate but a faster pace. That agrees with the expected general behavior for AE-based analysis methods, and this work seeks to confirm such a conclusion through the methods that are presented in Section 2, as summarized in Figure 14.

The b -value parameter (Figure 14a) was calculated in [27] by separating the dataset into packs of 25 signals, with five-signal overlaps between the successive packs. The sudden coefficient changes at $t \approx 0.6$ coincide with the avalanche that is observed in the signals count, confirming this point as critical for the test in question.

The long-range correlation results for the spaghetti bridge appear in Figure 14c. The calculation methodology is the same one that is used with the GFRP plate, but since this test has yielded fewer signal samples, a 6-signals moving window was used to compute α and H . Both parameters behave similarly until $t \approx 0.55$, with values of about 0.9 indicating persistent correlations. Then, they present significant local changes, most notably at normalized instants 0.6, 0.65, and 0.79, with the Hurst exponent appearing as more sensitive to the observed signal changes. Contrary to the GFRP plate case, no anti-persistent correlations are observed, just strong long-range correlations with local instabilities for the points of more significant AE activity.

Finally, the results for natural time analysis are presented in Figure 14d, considering $Q_k = A_{\max,k}^{1.5}$ and using the same calculation method that was described for the GFRP plate. A single coincidence point is identified at a normalized time 0.1206. If only the order parameters for criticality (κ_1 and $\langle D \rangle$) are considered, new convergence points are observed at the normalized instant 0.54, which is close to the already discussed sudden rise in AE energy at $t \approx 0.6$ (Figure 14b), which was also identified through the b -value (Figure 14a). The last convergence point occurs at $t = 0.62$, where the two exponents change behavior

again until the structure collapses. Subsequent analysis can show that these results do not change with respect to the amplitude threshold for identifying hits. Contrary to the GFRP plate, however, there is no discernible coincidence point in the vicinity of the structure's failure.

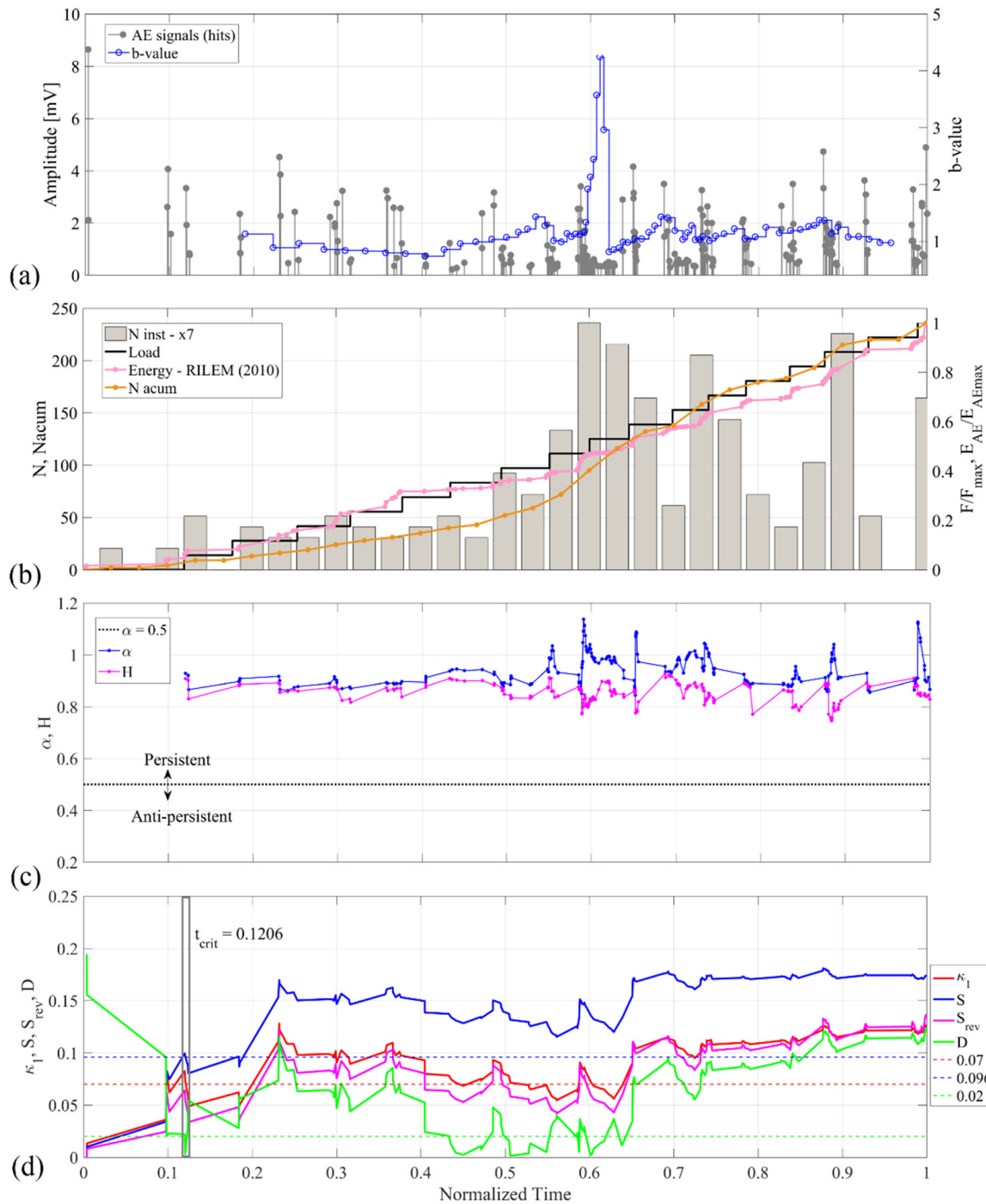


Figure 14. (a) The AE signals and corresponding b -values for the spaghetti bridge loading test, as described in [27]); (b) The numbers of instantaneous signals, the number of accumulated signals, the applied load, and the accumulated energy versus normalized time. The first was multiplied by 7 to maintain the same vertical scale for instantaneous and accumulated signals; (c) The application of Hurst and DFA methods to the AE data; (d) NT analysis of the AE time series (this figure's format follows that of Figure 7d).

3.2.3. Discussion

(i) As in the first application, important information was omitted during the first calculation of parameters H and α . For this reason, such a calculation was repeated for different time scales to further evaluate these parameters' usefulness in monitoring structural damage.

Figure 15 illustrates H and α for signals that were identified at normalized instants 0.59 and 0.65. The red line indicates the overall linear fit for the data, whereas the fits for each subset are shown in blue. The values for H and α are high for short-time ranges, i.e., high-frequency signals are persistent as expected from [48], whereas low-frequency ones ($n \geq 400$) are anti-persistent.

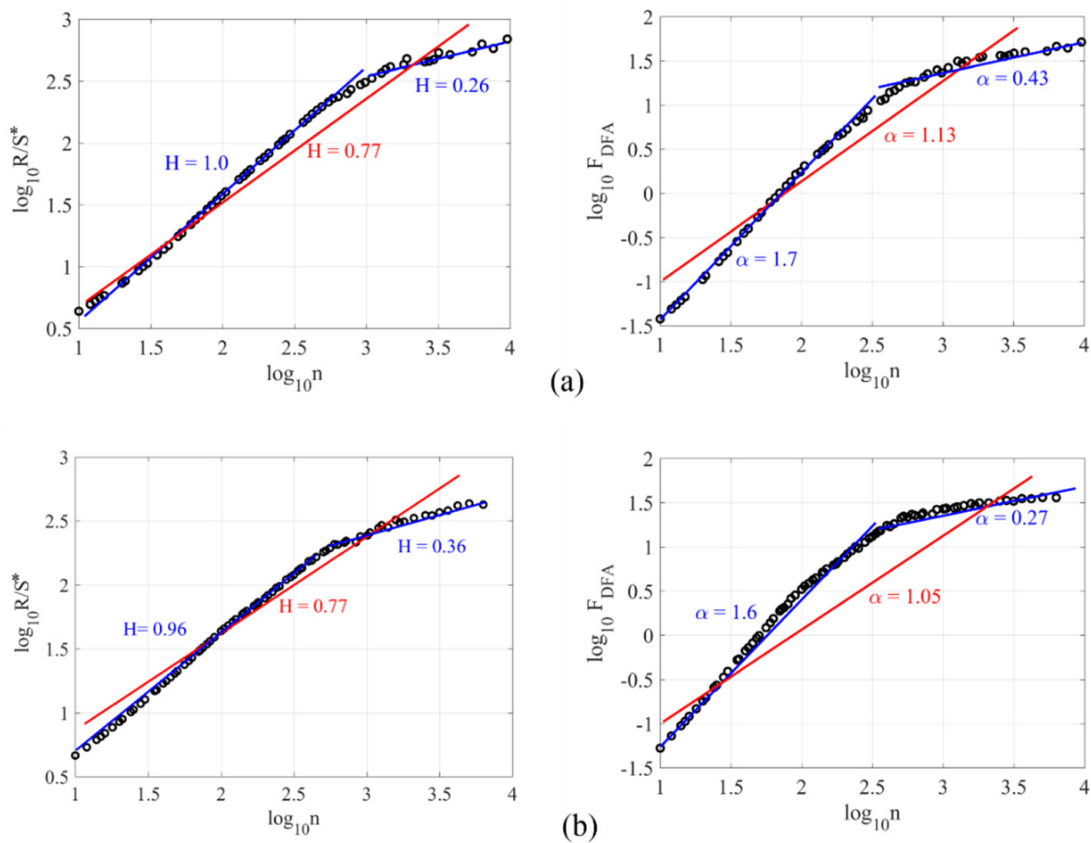


Figure 15. Details of the Hurst and DFA exponents for (a) signal #84 at normalized time 0.59; (b) signal #127 at normalized time 0.65.

Naming the DFA values for $n < 400$ e $n \geq 400$ as α_{short} and α_{high} , respectively, their behavior throughout time appears in Figure 16, where the AE signals' amplitudes are out of scale. As in the first application, these parameters have opposite tendencies as a high-AE-activity point is approached. While high-frequency correlations are always persistent, low-frequency ones are persistent for noncritical periods, turning into anti-persistent at critical points, such as at the normalized instant 0.6 and during the subsequent avalanches.

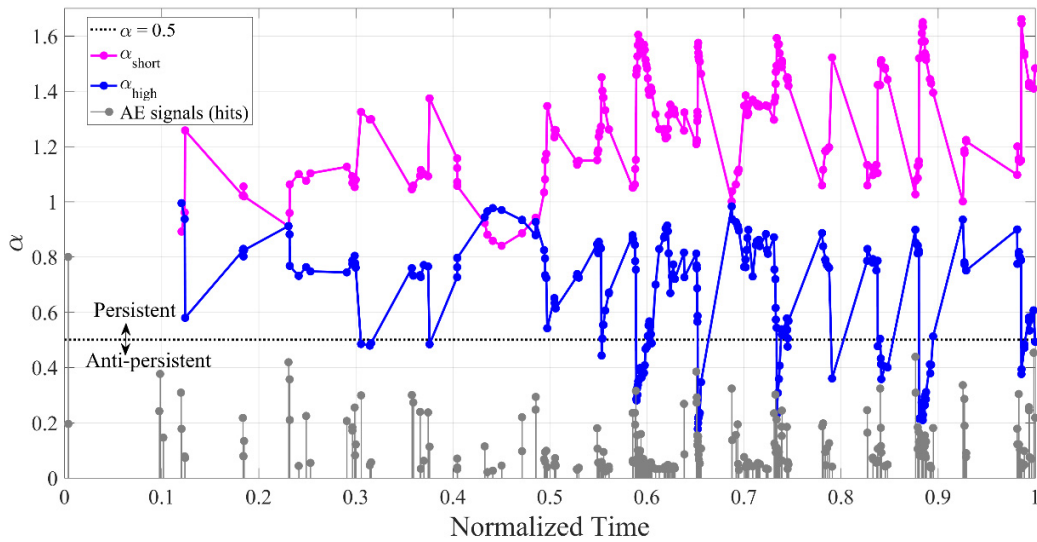


Figure 16. DFA results considering short (α_{short}) and large (α_{high}) time ranges for the spaghetti bridge. AE signals out of scale.

(ii) The natural time analysis of the spaghetti bridge’s AE results was also performed using $Q_k = E_{AE,k}$, as shown in Figure 17a. Now, two possibly critical points are identified, one at $t = 0.4046$ ($F/F_{max} = 0.3178$) and the other at $t = 0.6025$ ($F/F_{max} = 0.4695$), where the latter is followed by significant changes in both the order parameters and the two entropy metrics, anticipating the bridge collapse. Figure 17b depicts the normalized power spectrum $\Pi(\phi)$ versus the natural frequency (ϕ) that was calculated for the AE signal (blue), compared to its expected theoretical value (red). Once again, the criticality parameter $\Pi(\phi)$ appears as a good predictor of critical stages throughout the test.

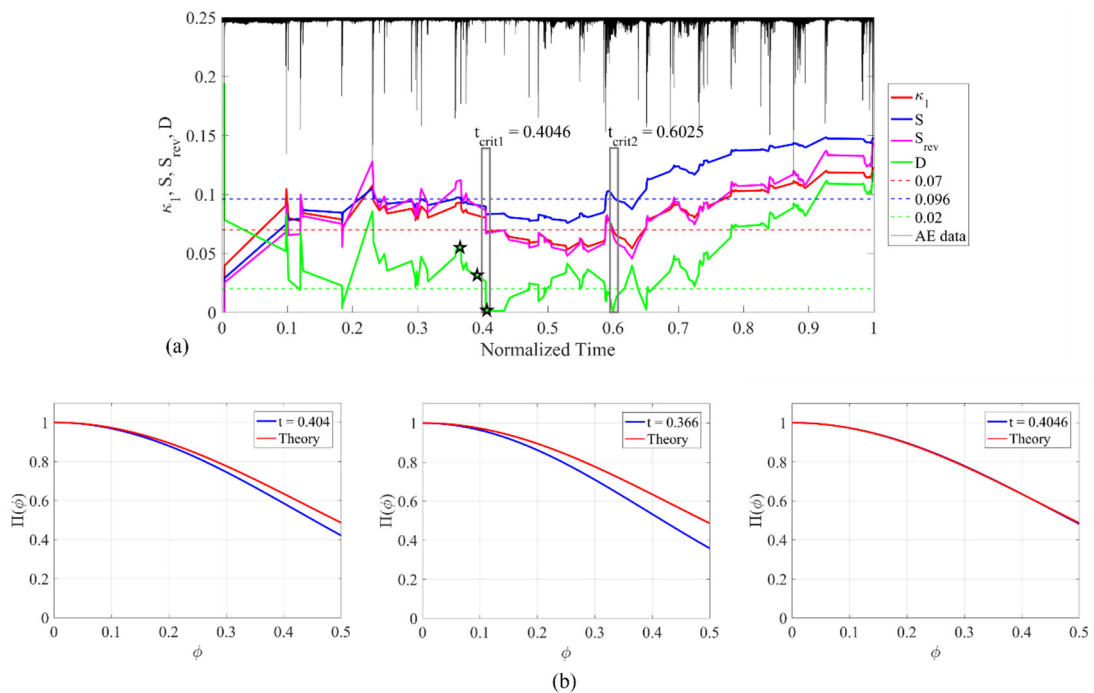


Figure 17. (a) Results from the natural time analysis of the AE events during the loading test for the spaghetti model bridge, according to the same format described for Figure 7d. (b) Evolution of $\Pi(\phi)$ during the same test.

4. Conclusions

This work focused on using time series methods to analyze acoustic emission data from two experimental tests with different materials: (i) a fiber-reinforced polymer plate undergoing a three-point bending test; (ii) a spaghetti bridge model from an undergraduate-level student loading contest. The time series analysis was carried out through two approaches: calculating DFA and Hurst exponents to characterize long-range correlations and analysis in the natural time domain. The purpose was to identify the possibility of using these methodologies to predict the critical points or failure in the studied structures. From the results, one concludes that:

- Both the Hurst and DFA exponents yielded very similar results, which indicate that no high-order trends are present in the data.
- For both applications, the DFA parameter that was calculated for the whole dataset was inconclusive. However, when considered separately, the low (α_{low}) and high (α_{high}) state levels indicated a critical region where one converged to extreme anti-persistent correlations, and the other, to extreme persistent ones. That highlights these parameters' usefulness in indicating the criticality of the structure.
- The analysis in the natural time domain showed that the convergence of the order parameters and the entropies could predict the structure's entry in a critical stage, whether it is calculated from the AE energy or from counting the ruptured samples.
- In both the analyzed examples it was possible to clearly perceive (see Figures 7, 9 and 11) the correlation between the critical interval that was determined by the DFA, R/S^* , NT, and the b -value analyses, from which the imminent increments in the acoustic emission activity follow.
- The indexes that were analyzed here, among others used the b -value which led to identifying when the damage process approaches a critical regime. In this situation, an unstable behavior is imminent and it is characterized by an increment in the global AE activity and in the amplitude of the AE signals. However, it is worth pointing out that it may also happen that, after reaching a critical phase with a large emission of energy, if the conditions of the damage continue to evolve in the structure, another stable one follows, which can be followed by another critical one, etc. Therefore, reaching a critical phase can always be correlated with local instability, but it is not always necessarily correlated with global structural failure. See, e.g., Ref. [14].

Author Contributions: Conceptualization, L.F.F., A.B.C., É.S.C., I.I., G.N. and G.L.; Methodology, L.F.F., É.S.C., B.N.R.T., I.I. and G.L.; Formal analysis, L.F.F., É.S.C. and I.I.; Investigation, L.F.F., É.S.C., A.B.C., B.N.R.T. and L.E.K.; Writing—original draft preparation, L.F.F., A.B.C., É.S.C., I.I. and M.S.; Writing—review and editing, L.F.F., B.N.R.T., I.I., L.E.K., G.L., G.N. and M.S.; Visualization, L.F.F. and I.I.; Supervision, L.E.K., G.N., G.L. and I.I. All authors have read and agreed to the published version of the manuscript.

Funding: This research was funded by CNPq and CAPES (Brazil), and the sponsorship guaranteed with basic research funds provided by Politecnico di Torino (Italy).

Institutional Review Board Statement: Not applicable.

Informed Consent Statement: Not applicable.

Acknowledgments: The authors wish to acknowledge the Brazilian National Council for Scientific and Technological Development (CNPq), the Coordination for the Improvement of Higher Level of Education Personnel (CAPES) and the sponsorship guaranteed with basic research funds provided by Politecnico di Torino, Italy for their financial aids in this work.

Conflicts of Interest: The authors declare no conflict of interest.

Nomenclature

N	Cumulative number of events/hits
A	Signal amplitude
A_{\max}	Maximum signal amplitude
b	b -value parameter
D, d	Fractal dimension
F_{DFA}	Average fluctuations in DFA
n	Window size
α	Angular coefficient of $\log F_{\text{DFA}} \propto \log n$
N_{\max}	Total number of points in the series
x	A time series
y	Integrate the time series
X	Sum the differences from the mean in Hurst analysis
R	Local range
S^*	Standard deviation
n_w	Total number of windows
H	Hurst exponent
n_{\min}	Smallest window size
n_{\max}	Largest window size
χ	Natural time
Q	Energy of the individual event
p	Normalized energy (Q)
κ_1	Natural time χ 's variance
S	Entropy in natural time
S_{rev}	Time-reversal entropy
$\langle D \rangle$	"Average" distance
ω	Natural angular frequency
ϕ	Frequency in natural time
Π	Normalized power spectrum
S_u	Entropy of uniform noise
E	Young's modulus
p	Mass density
α_{short}	Short-term windows
α_{high}	Long-term windows

References

1. Nemat-Nasser, S.; Hori, M. *Micromechanics: Overall Properties of Heterogeneous Materials (North-Holland Series in Applied Mathematics and Mechanics)*; Elsevier: Amsterdam, The Netherlands, 1999.
2. Torquato, S. *Random Heterogeneous Materials: Microstructure and Macroscopic Properties*; Springer: New York, NY, USA, 2013.
3. Gross, D.; Seelig, T. *Fracture Mechanics—With an Introduction to Micromechanics*; Mechanical Engineering Series; Springer: Berlin/Heidelberg, Germany, 2006.
4. Kachanov, L. Time of the rupture process under creep conditions. *Izvestiia Akademii Nauk SSSR* **1957**, *8*, 26–31.
5. Chaboche, J. Continuum damage mechanics: Present state and future trends. *Nucl. Eng. Des.* **1987**, *105*, 19–33. [[CrossRef](#)]
6. Voyiadjuis, G.Z. *Handbook of Damage Mechanics, Nano to Macro Scale for Materials and Structures*; Springer: Berlin/Heidelberg, Germany, 2014.
7. Daniels, H.E. The statistical theory of the strength of bundles of threads I. *Proc. R. Soc. Lond.* **1945**, *183*, 405–435.
8. Hansen, A.; Hemmer, P.C.; Pradhan, S. *The Fiber Bundle Model: Modeling Failure in Materials (Statistical Physics of Fracture and Breakdown)*; Wiley-VCH Verlag GmbH & Co. KGaA: Weinheim, Germany, 2015; ISBN 978-3-527-41214-3.
9. Jenabidehkordi, A. Computational methods for fracture in rock: A review and recent advances. *Front. Struct. Civ. Eng.* **2019**, *13*, 273–287. [[CrossRef](#)]
10. Grosse, C.U.; Ohtsu, M. *Acoustic Emission Testing*; Springer: Berlin/Heidelberg, Germany, 2008.
11. Aki, K. Scaling law of seismic spectrum. *J. Geophys. Res.* **1967**, *72*, 1217–1231. [[CrossRef](#)]
12. Carpinteri, A.; Lacidogna, G.; Puzzi, S. From criticality to final collapse: Evolution of the b -value from 1.5 to 1.0. *Chaos Solitons Fractals* **2009**, *41*, 843–853. [[CrossRef](#)]
13. Carpinteri, A.; Lacidogna, G.; Accornero, F. Fluctuations of 1/f Noise in Damaging Structures Analyzed by Acoustic Emission. *Appl. Sci.* **2018**, *8*, 1685. [[CrossRef](#)]

14. Carpinteri, A.; Lacidogna, G.; Corrado, M.; Di Battista, E. Cracking and Crackling in Concrete-Like Materials: A Dynamic Energy Balance. *Eng. Fract. Mech.* **2016**, *155*, 130–144. [[CrossRef](#)]
15. Alava, M.J.; Nukala, P.K.V.V.; Zapperi, S. Statistical models of fracture. *Adv. Phys.* **2006**, *55*, 349–476. [[CrossRef](#)]
16. Xu, D.; Liu, P.; Chen, Z.; Cai, Q.; Leng, J. Dynamic feature evaluation on streaming acoustic emission data for adhesively bonded joints for composite wind turbine blade. *Struct. Health Monit.* **2021**. [[CrossRef](#)]
17. Wilson, K.G. Problems in Physics with Many Scales of Length. *Sci. Am.* **1979**, *241*, 140–157. [[CrossRef](#)]
18. Tainter, J.A. *The Collapse of Complex Societies, New Studies in Archaeology*; Cambridge University Press: Cambridge, UK, 1988; ISBN 978-0-521-38673-9.
19. Rosser, J.B. The Rise and Fall of Catastrophe Theory Applications in Economics: Was the Baby Thrown Out with the Bathwater. *J. Econ. Dyn. Control.* **2007**, *31*, 3255–3280. [[CrossRef](#)]
20. Rundle, J.B.; Turcotte, D.L.; Shcherbakov, R.; Klein, W.; Sammis, C. Statistical physics approach to understanding the multiscale dynamics of earthquake fault systems. *Rev. Geophys.* **2003**, *41*, 1019–1041. [[CrossRef](#)]
21. Turcotte, D.L.; Newman, W.I.; Shcherbakov, R. Micro and Macroscopic Models of Rock Fracture. *Geophys. J. Int.* **2003**, *152*, 718–728. [[CrossRef](#)]
22. Hurst, H.E. Long-term storage capacity of reservoirs. *Trans. Am. Soc. Civ. Eng.* **1951**, *116*, 770–808. [[CrossRef](#)]
23. Peng, C.K.; Buldyrev, S.V.; Havlin, S.; Simons, M.; Stanley, H.E.; Goldberger, A.L. Mosaic Organization of DNA Nucleotides. *Phys. Rev. E* **1994**, *49*, 1685–1689. [[CrossRef](#)]
24. Varotsos, P.A.; Sarlis, N.V.; Skordas, E.S. Spatio-temporal complexity aspects on the interrelation between seismic electric signals and seismicity. *Pract. Athens Acad.* **2001**, *76*, 294–321.
25. Potirakis, S.M.; Karadimitrakakis, A.; Eftaxias, K. Natural time analysis of critical phenomena: The case of pre-fracture electromagnetic emissions. *Chaos* **2013**, *23*, 023117. [[CrossRef](#)]
26. Friedrich, L.; Colpo, A.; Maggi, A.; Becker, T.; Lacidogna, G.; Iturrioz, I. Damage process in glass fiber reinforced polymer specimens using acoustic emission technique with low frequency acquisition. *Compos. Struct.* **2021**, *256*, 113105. [[CrossRef](#)]
27. Tanzi, R.B.N.; Sobczyk, M.; Becker, T.; González, L.A.S.; Vantadori, S.; Iturrioz, I.; Lacidogna, G. Damage Evolution Analysis in a “Spaghetti” Bridge Model Using the Acoustic Emission Technique. *Appl. Sci.* **2021**, *11*, 2718. [[CrossRef](#)]
28. Sagasta, F.; Zitto, M.E.; Piotrkowski, R.; Benavent-Climent, A.; Suarez, E.; Gallego, A. Acoustic emission energy b-value for local damage evaluation in reinforced concrete structures subjected to seismic loadings. *Mech. Syst. Signal Processing* **2018**, *102*, 262–277. [[CrossRef](#)]
29. Richter, C.F. *Elementary Seismology*; W. H. Freeman and Company: London, UK, 1958.
30. Carpinteri, A.; Lacidogna, G.; Nicolini, G. Fractal analysis of damage detected in concrete structural elements under loading. *Chaos Solitons Fractals* **2009**, *42*, 2047–2056. [[CrossRef](#)]
31. Varotsos, P.A.; Sarlis, N.V.; Skordas, E.S. Detrended fluctuation analysis of the magnetic and electric field variations that precede rupture. *Chaos Interdiscip. J. Nonlinear Sci.* **2009**, *19*, 023114. [[CrossRef](#)] [[PubMed](#)]
32. Kantelhardt, J.W.; Koscielny-Bunde, E.; Rego, H.H.A.; Havlin, S.; Bunde, A. Detecting long-range correlations with detrended fluctuation analysis. *Phys. A Stat. Mech. Its Appl.* **2001**, *295*, 441–454. [[CrossRef](#)]
33. Mandelbrot, B.B. *The Fractal Geometry of Nature*; W. H. Freeman and Company: New York, NY, USA, 1982.
34. Filho, A.M.; da Silva, M.F.; Zebende, G.F. Autocorrelation and cross-correlation in time series of homicide and attempted homicide. *Phys. A Stat. Mech. Its Appl.* **2014**, *400*, 12–19. [[CrossRef](#)]
35. Coronado, A.V.; Carpena, P. Size Effects on Correlation Measures. *J. Biol. Phys.* **2005**, *31*, 121–133. [[CrossRef](#)]
36. Talkner, P.; Weber, R.O. Power spectrum and detrended fluctuation analysis: Application to daily temperatures. *Phys. Rev. E* **2000**, *62*, 150–160. [[CrossRef](#)]
37. Rigoli, L.M.; Lorenz, T.; Coey, C.; Kallen, R.; Jordan, S.; Richardson, M.J. Co-actors Exhibit Similarity in Their Structure of Behavioural Variation That Remains Stable Across Range of Naturalistic Activities. *Sci. Rep.* **2020**, *10*, 6308. [[CrossRef](#)]
38. Hu, K.; Ivanov, P.C.; Chen, Z.; Carpena, P.; Stanley, H.E. Effect of trends on detrended fluctuation analysis. *Phys. Rev. E Stat. Nonlin. Soft. Matter Phys.* **2001**, *64*, 011114. [[CrossRef](#)]
39. Landa, E.; Morales, I.O.; Fossion, R.; Stránský, P.; Velázquez, V.; Vieyra, J.C.L.; Frank, A. Criticality and long-range correlations in time series in classical and quantum systems. *Phys. Rev. E* **2011**, *84*, 016224. [[CrossRef](#)]
40. Damouras, S.; Chang, M.D.; Sejdić, E.; Chau, E. An empirical examination of detrended fluctuation analysis for gait data. *Gait Posture* **2010**, *31*, 336–340. [[CrossRef](#)] [[PubMed](#)]
41. Mariani, M.C.; Asante, P.K.; Bhuiyan, M.A.M.; Beccar-Varela, M.P.; Jaroszewicz, S.; Tweneboah, O.K. Long-Range Correlations and Characterization of Financial and Volcanic Time Series. *Mathematics* **2020**, *8*, 441. [[CrossRef](#)]
42. Basingthwaighte, J.B.; Raymond, G.M. Evaluating rescaled range analysis for time series. *Ann. Biomed. Eng.* **1994**, *22*, 432–444. [[CrossRef](#)] [[PubMed](#)]
43. Li, J.; Chen, Y. Rescaled range (R/S) analysis on seismic activity parameters. *Acta Seismol. Sin.* **2001**, *14*, 148–155. [[CrossRef](#)]
44. Varotsos, P.A.; Sarlis, N.V.; Skordas, E.S. Long-range correlations in the electric signals that precede rupture. *Phys. Rev. E* **2002**, *66*, 011902. [[CrossRef](#)] [[PubMed](#)]

45. Hausdorff, J.M.; Mitchell, S.L.; Firtion, R.; Peng, C.-K.; Cudkowitz, M.E.; Wei, J.Y.; Goldberger, A.L. Altered fractal dynamics of gait: Reduced stride-interval correlations with aging and Huntington's disease. *J. Appl. Physiol.* **1997**, *82*, 262–269. [[CrossRef](#)]
46. Jordan, K.; Challis, J.H.; Newell, K.M. Long range correlations in the stride interval of running. *Gait Posture* **2006**, *24*, 120–125. [[CrossRef](#)]
47. Niccolini, G.; Manuello, A.; Marchis, E.; Carpinteri, A. Signal frequency distribution and natural-time analysis from acoustic emission monitoring of an arched structure in the Castle of Raconigi. *Nat. Hazards Earth Syst. Sci.* **2017**, 1025–1032. [[CrossRef](#)]
48. Varotsos, P.A.; Panayiotis, A.; Sarlis, N.V.; Skordas, E.S. *Natural Time Analysis: The New View of Time*; Springer: Berlin/Heidelberg, Germany, 2011. [[CrossRef](#)]
49. Loukidis, A.; Perez-Oregon, J.; Pasiou, E.D.; Sarlis, N.V.; Triantis, D. Similarity of fluctuations in critical systems: Acoustic emissions observed before fracture. *Phys. A Stat. Mech. Appl.* **2021**, *566*, 125622. [[CrossRef](#)]
50. Ramírez-Rojas, A.; Flores-Márquez, E.L. Order parameter analysis of seismicity of the Mexican Pacific coast. *Phys. A Stat. Mech. Appl.* **2013**, *392*, 2507–2512. [[CrossRef](#)]
51. Shannon, C.E. A mathematical theory of communication. *Bell Syst. Tech. J.* **1948**, *27*, 379–423. [[CrossRef](#)]
52. Potirakis, S.M.; Mastrogiannis, D. Critical features revealed in acoustic and electromagnetic emissions during fracture experiments on LiF. *Phys. A Stat. Mech. Appl.* **2017**, *485*, 11–12. [[CrossRef](#)]
53. Daniel, S.H. Seismic electric signals (SES) and earthquakes: A review of an updated VAN method and competing hypotheses for SES generation and earthquake triggering. *Phys. Earth Planet. Inter.* **2020**, *302*, 106484.
54. Varotsos, P.A.; Panayiotis, A.; Sarlis, N.V.; Skordas, E.S. Long-range correlations in the electric signals that precede rupture: Further investigations. *Phys. Rev. E* **2003**, *67*, 021109. [[CrossRef](#)]
55. Varotsos, P.A.; Tanaka, H.K.; Sarlis, N.V.; Skordas, E.S. Similarity of fluctuations in correlated systems: The case of seismicity. *Phys. Rev. E* **2005**, *72*, 041103. [[CrossRef](#)]
56. Varotsos, P.A.; Sarlis, N.V.; Skordas, E.S.; Tanaka, H.K.; Lazaridou, M.S. Attempt to distinguish long-range temporal correlations from the statistics of the increments by natural time analysis. *Phys. Rev. E* **2006**, *74*, 021123. [[CrossRef](#)]
57. Niccolini, G.; Potirakis, S.M.; Lacidogna, G.; Borla, O. Criticality Hidden in Acoustic Emissions and in Changing Electrical Resistance during Fracture of Rocks and Cement-Based Materials. *Materials* **2020**, *13*, 5608. [[CrossRef](#)]
58. Akovali, G. *Handbook of Composite Fabrication*; Rapra Tech Ltd.: Shrewsbury, UK, 2001.
59. Imap. Available online: <https://imap.com.br> (accessed on 20 March 2020).
60. RILEM Technical Committee. Recommendation of RILEM TC 212-ACD: Acoustic emission and related NDE techniques for crack detection and damage evaluation in concrete: Test method for classification of active cracks in concrete structures by acoustic emission. *Mater. Struct.* **2010**, *43*, 1187–1189.
61. Skordas, E.S.; Christopoulos, S.R.G.; Sarlis, N.V. Detrended fluctuation analysis of seismicity and order parameter fluctuations before the M7.1 Ridgecrest earthquake. *Nat. Hazards* **2020**, *100*, 697–711. [[CrossRef](#)]
62. Carpinteri, A.; Niccolini, G.; Lacidogna, G. Time Series Analysis of Acoustic Emissions in the Asinelli Tower during Local Seismic Activity. *Appl. Sci.* **2018**, *8*, 1012. [[CrossRef](#)]
63. Kanamori, H.; Anderson, D.L. Theoretical basis of some empirical relationships in seismology. *Bull. Seismol. Soc. Am.* **1975**, *65*, 1073–1095.
64. Hloupis, G.; Stavrakas, I.; Pasiou, E.D.; Triantis, D.; Kourkoulis, S.K. Natural Time Analysis of Acoustic Emissions in Double Edge Notched Tension (DENT) Marble Specimens. *Procedia Eng.* **2015**, *109*, 248–256. [[CrossRef](#)]
65. Hloupis, G.; Stavrakas, I.; Vallianatos, F.; Triantis, D. A preliminary study for prefailure indicators in acoustic emissions using wavelets and natural time analysis. *Proc. Inst. Mech. Eng. Part L J. Mater. Des. Appl.* **2016**, *230*, 780–788. [[CrossRef](#)]
66. Lin, A.-J.; Shang, P.-J.; Zhou, H.-C. Effects of Exponential Trends on Correlations of Stock Markets. *Math. Probl. Eng.* **2014**, *2014*, 340845. [[CrossRef](#)]
67. Silva, F.E.; Gonçalves, L.L.; Ferreira, D.B.B.; Rebello, J.M.A. Characterization of failure mechanism in composite materials through fractal analysis of acoustic emission signals. *Chaos Solitons Fractals* **2005**, *26*, 481–494. [[CrossRef](#)]
68. Loukidis, A.; Pasiou, E.D.; Sarlis, N.V.; Triantis, D. Fracture analysis of typical construction materials in natural time. *Phys. A Stat. Mech. Appl.* **2020**, *547*, 123831. [[CrossRef](#)]
69. González, S.L.A.; Morsch, I.B.; Masuero, J.R. Didactic Games in Engineering Teaching—Case: Spaghetti Bridges Design and Building Contest. In Proceedings of the 18th International Congress of Mechanical Engineering (COBEM 2005), Ouro Preto, MG, Brazil, 6–11 November 2005.